

Version 1.0 as of June 9, 2021

Primary authors: Claudio Durastanti, Yabebal T. Fantaye, Frode K. Hansen, Domenico Marinucci, Isaac Z. Pesenson  
To be submitted to Physical Review D

*DØ INTERNAL DOCUMENT – NOT FOR PUBLIC DISTRIBUTION*

## A Simple Proposal for Radial 3D Needlets

C. Durastanti,<sup>1,\*</sup> Y. Fantaye,<sup>1,†</sup> F. Hansen,<sup>2,‡</sup> D. Marinucci,<sup>1,§</sup> and I. Z. Pesenson<sup>3,¶</sup>

<sup>1</sup>*Dipartimento di Matematica, Universit di Roma”Tor Vergata,  
” Via della Ricerca Scientifica 1, I-00133 Roma, Italy*

<sup>2</sup>*Institute of Theoretical Astrophysics, University of Oslo, PO Box 1029 Blindern, 0315 Oslo, Norway*

<sup>3</sup>*Department of Mathematics, Temple University, Philadelphia, PA 19122*

(Dated: June 9, 2021)

We present here a simple construction of a wavelet system for the three-dimensional ball, which we label *Radial 3D Needlets*. The construction envisages a data collection environment where an observer located at the centre of the ball is surrounded by concentric spheres with the same pixelization at different radial distances, for any given resolution. The system is then obtained by weighting the projector operator built on the corresponding set of eigenfunctions, and performing a discretization step which turns out to be computationally very convenient. The resulting wavelets can be shown to have very good localization properties in the real and harmonic domain; their implementation is computationally very convenient, and they allow for exact reconstruction as they form a tight frame systems. Our theoretical results are supported by an extensive numerical analysis.

PACS numbers: 98.80.-k, 95.75.Mn, 07.05.Rm

### I. INTRODUCTION

The last decade has represented a golden era for Cosmology: a flood of data with unprecedented accuracy has become available on such diverse fields as Cosmic Microwave Background (WMAP, Planck, SPT, ACT, see for instance [6, 9, 23, 49] and references therein), Ultra High Energy Cosmic Rays (cfr. [46]), Gamma rays (Fermi, Agile, ARGO-YBJ+, cfr. [2, 16, 21]), neutrinos (cfr. [1]) and many others. Many of these experiments have produced full-sky surveys, and basically all of them have been characterized by fields of views covering thousands of square degrees. In such circumstances, data analysis methods based on flat sky approximations have become unsatisfactory, and a large amount of effort has been devoted to the development of procedures which take fully into account the spherical nature of collected data.

As well-known, Fourier analysis is an extremely powerful method for data analysis and computation; in a spherical context, Fourier analysis corresponds to the spherical harmonics dictionary, which is now fully implemented in very efficient and complete packages such as HealPix, see [22]. For most astrophysical applications, however, stan-

dard Fourier analysis may often result to be inadequate due to the lack of localization properties in the real domain; because of this, spherical harmonics cannot handle easily the presence of huge regions of masked data, nor they can be used to investigate local features such as asymmetries and anisotropies or the search for point sources.

As a consequence, several methods based on spherical wavelets have become quite popular in astrophysical data analysis, see for instance [7, 13, 14, 33, 34, 47, 48, 53, 57, 58] and also [59] for a review. These procedures have been applied to a huge variety of different problems, including for instance point source detection in Gamma ray data (cfr. [25, 55]), testing for nonGaussianity (cfr. [13, 28, 50, 53]), searching for asymmetries and local features (cfr. [8, 48, 60]), point source subtraction on CMB data (see [54]), map-making and component separation (cfr. [5, 11, 37, 51]), and several others.

The next decade will probably experience an even more amazing improvement on observational data. Huge surveys are being planned or are already at the implementation stage, many of them aimed at the investigation of the large scale structure of the Universe and the investigation of Dark Energy and Dark Matter; for instance, a large international collaboration is fostering the implementation of the Euclid satellite mission, aimed at a deep analysis of weak gravitational lensing on nearly half of the celestial sky (see for instance [30]). These observational data are also complemented by N-body simulation efforts (cfr. [56]) aimed at the generation of realistic three-dimensional model of the current large scale structure of the Universe. From the point of view of data analysis, these data naturally entail a three-dimensional structure,

---

\*Electronic address: [durastan@axp.mat.uniroma2.it](mailto:durastan@axp.mat.uniroma2.it); supported by the ERC grant *Pascal* 277742

†Electronic address: [fantaye@axp.mat.uniroma2.it](mailto:fantaye@axp.mat.uniroma2.it); supported by the ERC grant *Pascal* 277742

‡Electronic address: [f.k.hansen@astro.uio.no](mailto:f.k.hansen@astro.uio.no)

§Electronic address: [marinucc@mat.uniroma2.it](mailto:marinucc@mat.uniroma2.it); partially supported by the ERC grant *Pascal* 277742

¶Electronic address: [pesenson@temple.edu](mailto:pesenson@temple.edu)

which calls for suitable techniques of data analysis.

In view of the previous discussion, it is easy to understand the motivation to develop wavelet systems on the three-dimensional ball, extending those already available on the sphere. Indeed, some important efforts have already been spent in this direction, especially in the last few years. Some attempts outside the astrophysical community have been provided by [15, 36, 45]; however the first two proposals are developed in a continuous setting and do not seem to address discretization issues and the implementation of an exact reconstruction formula. On the other hand in [45] the authors proceed by projecting the three-dimensional ball into a unit sphere in four dimension, and then developing the corresponding spherical needlet construction in the latter space. While this approach is mathematically intriguing, to the best of our knowledge it has not led to a practical implementation, at least in an astrophysical context. This may be due to some difficulties in handling the required combination of Jacobi polynomials, and the lack of explicit recipes for cubature points in this context; moreover the projection of the unit ball on a unit sphere in higher dimension may induce some local anisotropies, whose effect still needs to be investigated in an astrophysical context.

Within the astrophysical community, some important proposals for the construction of three-dimensional wavelets have been advocated by [29] and [31]. In the former paper, the authors propose to use a frequency filter on the Fourier-Bessel transform of the three-dimensional field. The proposal by [31] also concentrates on Fourier-Bessel transforms, and is mainly aimed at the construction of a proper set of cubature points and weights on the radial part. This is in practice a rather difficult task: while it is theoretically known that the cubature points can be taken to be the zeroes of Bessel functions of increasing degrees, in practice these points are not available explicitly and the related computations may be quite challenging. To overcome this issue, in [31] a very interesting solution is advocated: more precisely, the authors start by constructing an exact transform on the radial part using damped Laguerre polynomials, which allow for an exact quadrature rule. Combining this procedure with the standard spherical transform, they obtain an exact 3-dimensional decomposition named Fourier-Laguerre transform. Their final proposal, the so-called flaglet transform, is then obtained by an explicit projection onto the Bessel family (e.g., a form of harmonic tiling on the Fourier-Laguerre transform); this approach is computationally feasible and exhibits very good accuracy properties from the numerical point of view.

Our starting point here is to some extent related, and quite explicitly rooted in the astrophysical applications we have in mind. In particular, we envisage a situation where an observer located at the centre of a ball is collecting data, e.g., we assume that she/he is observing a family of concentric spheres centred at the origin. At a given resolution level, the pixelization on each of these spheres is assumed to be the same, no matter their ra-

dial distance from the origin - this seems a rather realistic representation of astrophysical experiments, although of course it implies that with respect to Euclidean distance the sampling is finer for points located closer to the observer. In this sense, our construction has an implicit radial symmetry which we exploit quite fully: in particular, we view the ball of radius  $R$  as a manifold  $M = [0, R] \times S^2$ , and we modify the standard spherical Laplacian so that the distance between two points on the same spherical shell depends only on the angular component and not on the radius of the shell. The corresponding eigenfunctions have very simple expressions in terms of trigonometric polynomials and spherical harmonics; our system (which we label *3D radial needlets*) is then built out of the same procedures as for needlets on the sphere, namely convolution of a projection operator by means of a smooth window function  $b(\cdot)$ , and discretization by means of an explicitly provided set of cubature points. Concerning the latter, cubature points and weights arise very simply from the tensor products of cubature points on the sphere (as provided by HealPix in [22], for instance), and a uniform discretization on the radial part, which is enough for exact integration of trigonometric polynomials.

We believe the present proposals enjoys some important advantages, such as

1. very good localization properties (in the suitable distance, as motivated before); these properties can be established in a fully rigorous mathematical way, exploiting previous results on the construction of wavelets for general compact manifolds in [18], see also [44];
2. an exact reconstruction formula for band-limited functions, a consequence of the so-called tight frame property; the latter property has independent interest, for instance for the estimation of a binned spectral density by means of needlet coefficients (see [4] for analogous results in the spherical case);
3. a computationally simple and effective implementation scheme, entailing uniform discretization and the exploitation of existing packages;
4. a natural embedding into experimental designs which appear quite realistic from an astrophysical point of view, as discussed earlier.

The construction and these properties are discussed in more details in the rest of this paper; we note that the same ideas can be simply extended to cover the case of spin valued functions, along the same lines as done for standard 2D needlets by [19, 20]: these extensions may be of interest to cover forthcoming data on weak gravitational lensing (e.g. [30]).

The paper is divided as follows: Section 2 presents the background material on our embedding of the three-dimensional ball, related Fourier analysis and discretiza-

tion issues; Section 3 presents the 3D radial needlets construction in details; Section 4 discusses the comparison with possible alternative proposals; Section 5 presents our numerical evidence, while some technical computations are collected in the Appendix.

## II. THE BASIC FRAMEWORK

As mentioned in the Introduction and discussed at length also in other papers ([27, 31]), in an astrophysical framework data collection on the ball is characterized by a marked asymmetry between the radial part and the spherical component. Indeed, it is well-known that for astrophysical datasets observations at a growing radial distance corresponds to events at higher redshift, which have hence occurred further away in time, not only in space; data at different redshifts correspond at different epochs of the Universe and are hence the outcome of different physical conditions. From the experimental point of view, the signal-to-noise ratio is strongly influenced by radial distance; for instance, a strong selection bias is introduced as higher and higher intrinsic luminosity is needed to observe objects at growing redshift. The asymmetry between the radial and spherical components is also reproduced in data storing mechanisms, which typically adopt independent discretization/pixelization schemes for the two components.

In view of these considerations, it seems natural and convenient to represent functions/observations on the three-dimensional ball  $\mathcal{B}_R = \{(x_1, x_2, x_3) : x_1^2 + x_2^2 + x_3^2 \leq R\}$  as being defined on a family of concentric spheres (shells), indexed by a continuous radial parameter (i.e., a growing redshift); here, the radius  $R$  of the ball can be taken to represent the highest redshift value  $z$  in the catalogue being analyzed,  $R = z_{\max}$ . In the sequel, we shall work with spherical coordinates  $(r, \theta, \varphi)$ ; for notational convenience, we take  $r = 2\pi z/R$ , so that  $r \in [0, 2\pi]$ . Formally, this means we shall focus on the product space

$$L^2(M, d\mu) = L^2([0, 2\pi], dr) \otimes L^2(S^2, d\sigma) ,$$

where  $d\mu = dr d\sigma$ ,  $d\sigma = (4\pi)^{-1} \sin \theta d\phi$  and  $dr$  denotes standard Lebesgue measure on the unit interval. This simplifying step is at the basis of our construction; indeed, for our purposes it will hence be sufficient to construct a tight and localized frame on  $L^2(M, d\mu)$ , a task which can be easily accomplished as follows.

Recall first that for square-integrable functions on the sphere, e.g. on  $L^2(S^2, d\sigma)$ , a standard orthonormal basis is provided by the set of spherical harmonics

$$\{Y_{\ell, m}(\theta, \phi)\} , \quad \ell = 0, 1, 2, \dots, m = -\ell, \dots, \ell ,$$

where  $\theta \in [0, \pi]$  and  $\varphi \in [0, 2\pi)$ . As well-known, the spherical harmonics provide a complete set of eigenfunctions for the spherical Laplacian

$$\Delta_{S^2} = \frac{1}{\sin \theta} \frac{\partial}{\partial \theta} \left( \sin \theta \frac{\partial}{\partial \theta} \right) + \frac{1}{\sin^2 \theta} \frac{\partial}{\partial \varphi} ,$$

indeed

$$\Delta_{S^2} Y_{\ell, m} = -\ell(\ell + 1) Y_{\ell, m} , \quad \ell = 1, 2, \dots$$

Hence, for any  $f \in L^2(S^2, d\sigma)$ , we have

$$f(\omega) = \sum_{\ell \geq 0} \sum_{m=-\ell}^{\ell} a_{\ell, m} Y_{\ell, m}(\omega) , \quad \omega \in S^2 ,$$

where the coefficients  $\{a_{\ell m}\}$  are evaluated by

$$a_{\ell, m} = \int_{S^2} \bar{Y}_{\ell, m}(\omega) f(\omega) \sigma(d\omega) .$$

On the other hand, for the radial part we consider the standard Laplacian operator  $\frac{\partial^2}{\partial r^2}$ , for which an orthonormal family of eigenfunctions is well-known to be given, for  $n = 0, 1, 2, \dots$ , by

$$\frac{\partial^2}{\partial r^2} (2\pi)^{-\frac{1}{2}} \exp(inr) = -n^2 (2\pi)^{-\frac{1}{2}} \exp(inr) .$$

We can hence define a Laplacian on  $M$  by

$$\Delta_M := \frac{\partial^2}{\partial r^2} + \Delta_{S^2} ,$$

e.g.

$$\Delta_M (\exp(inr) Y_{\ell m}(\omega)) = -e_{n, \ell} \exp(inr) Y_{\ell m}(\omega) , \quad (\text{II.1})$$

where

$$e_{n, \ell} = (n^2 + \ell(\ell + 1)) .$$

It is interesting to compare the action of  $\Delta_M$  with the standard Laplacian in spherical coordinates, which is given by

$$\Delta = \frac{1}{r^2} \frac{\partial}{\partial r} r^2 \frac{\partial}{\partial r} + \frac{1}{r^2} \Delta_{S^2} ; \quad (\text{II.2})$$

it can be checked that  $\Delta_M$  is the Laplace-Beltrami operator which correspond to the metric tensor

$$g_M = \begin{pmatrix} 1 & 0 & 0 \\ 0 & 1 & 0 \\ 0 & 0 & \sin^2 \theta \end{pmatrix} ,$$

as opposed to the usual Euclidean metric in spherical coordinates

$$g = \begin{pmatrix} 1 & 0 & 0 \\ 0 & r^2 & 0 \\ 0 & 0 & r^2 \sin^2 \theta \end{pmatrix} .$$

Likewise, the intrinsic distance between points  $x_1 = (r_1, \omega_1) = (r_1, \theta_1, \varphi_1)$  and  $x_2 = (r_2, \omega_2) = (r_2, \theta_2, \varphi_2)$ ,  $\omega_1, \omega_2 \in S^2$ ,  $r_1, r_2 \in [0, 2\pi]$ ,  $x_1, x_2 \in M$ , is provided by

$$d_M(x_1, x_2) = \sqrt{(r_1 - r_2)^2 + d_{S^2}^2(\omega_1, \omega_2)} , \quad (\text{II.3})$$

as opposed to Euclidean distance in spherical coordinates

$$d(x_1, x_2) = \sqrt{(r_1 - r_2)^2 + r_1 r_2 d_{S^2}^2(\omega_1, \omega_2)} . \quad (\text{II.4})$$

In words, in our setting the distance between two points at a given redshift is simply equal to their angular separation, whatever the redshift; on the contrary, under the Euclidean distance for a given angular separation the actual distance grows with the radial component. It can be argued that the metric  $d_M(\cdot, \cdot)$  is a natural choice for any wavelet construction where the radial component is decoupled from the spherical one. Given this choice of metric, our construction can be advocated as optimal, in the sense that it is based on the eigenfunctions of the associated Laplacian, and hence can be shown to enjoy excellent localization properties in the real and harmonic domains.

As a consequence of the previous discussion, the family of functions

$$u_{\ell, m, n}(r, \vartheta, \phi) = (2\pi)^{-\frac{1}{2}} \exp(inr) Y_{\ell, m}(\vartheta, \phi) \quad (\text{II.5})$$

provides an orthonormal basis on  $L^2(M, d\mu)$ , e.g., for any  $F \in L^2(M, d\mu)$ , the following expansion holds in  $L^2(M, d\mu)$ :

$$F(r, \vartheta, \phi) = \sum_{\ell \geq 0} \sum_{m=-\ell}^{\ell} \sum_{n \geq 0} a_{\ell, m, n} u_{\ell, m, n}(r, \vartheta, \phi) , \quad (\text{II.6})$$

where

$$\begin{aligned} a_{\ell, m, n} &:= \langle F, u_{\ell, m, n} \rangle_{L^2(M, d\mu)} \\ &= \int_M F(x) \bar{u}_{\ell, m, n}(x) d\mu(x) . \end{aligned} \quad (\text{II.7})$$

Of course, we can also rewrite (II.1) more compactly as

$$\Delta_M u_{\ell, m, n} = -e_{\ell, n} u_{\ell, m, n} . \quad (\text{II.8})$$

It may be noted that by taking a trigonometric basis for the radial part, we are implicitly assuming that the functions to reconstruct satisfy periodic boundary conditions. For astrophysical applications, this does not seem to bring in any problem. Indeed, we envisage circumstances where catalogues are provided within some band of redshift values  $0 < z_{min} < z_{max}$ ; periodicity is then obtained by simply padding zero observations at the boundaries.

The final step we need to complete our frame construction is discretization; the procedure is standard, and can be outlined as follows. Let  $\Pi_\Lambda$  be the a set of band-limited functions of order smaller than  $\Lambda$ , i.e. the linear span of the basis elements  $\{u_{\ell, m, n}\}$  for which the corresponding eigenvalues are such that  $e_{\ell, n} \leq \Lambda$ . Given an integer  $j$ , there exists a set of points and weights  $\aleph_j := \{\xi_{j, q, k} = (r_{j, q}, \theta_{j, k}, \varphi_{j, k})\}$ , and positive weights  $\{\lambda_{j, q, k}\}$ ,  $1 \leq q \leq Q_j$ ,  $1 \leq k \leq K_j$ , such that for all  $P \in$

$\Pi_{B^{2j+2}}$  the following exact cubature formula holds:

$$\begin{aligned} \int_M P(x) d\mu(x) &= \int_{S^2} \int_0^1 P(r, \theta, \varphi) dr d\sigma(\theta, \varphi) \\ &= \sum_{q=1}^{Q_j} \sum_{k=1}^{K_j} P(r_{j, q}, \theta_{j, k}, \varphi_{j, k}) \lambda_{j, q} \end{aligned} \quad (\text{II.9})$$

where the cubature points and weights satisfy

$$\lambda_{j, q, k} \approx B^{-3j} , K_j \approx B^{2j} , Q_j \approx B^j ,$$

and the notation  $x_1 \approx x_2$  means that there exists  $c > 0$  such that  $c^{-1}x_1 \leq x_2 \leq cx_1$ . More explicitly,  $K_j$  denotes the pixel cardinality on the spherical part, and  $Q_j$  represents the pixel cardinality on the radial part for a given resolution level  $j$ . In words, this means that for such functions integrals can be evaluated by finite sums over suitable points without any loss of accuracy. The existence of cubature points with the required properties follows immediately by the tensor construction which we described in the previous subsection: in particular, the spherical component  $(\theta_{j, k}, \varphi_{j, k})$  can be provided along the same scheme as in [39], while for practical applications the highly popular pixelization scheme provided by HealPix (cfr. [22]) may be used; on the radial part, cubature points maybe simply taken to be given by  $r_{j, q} := \frac{2\pi q}{B^j}$ ,  $q = 0, \dots, [B^j] - 1$ , where  $[\cdot]$  denotes the integer part, cfr. Section V.

### III. 3D RADIAL NEEDLETS AND THEIR MAIN PROPERTIES

Having set the basic framework for Fourier analysis and discretization on  $L^2(M, d\mu)$ , the construction of 3D radial needlets can proceed along very much the same lines as on the sphere or other manifolds (compare [38–42, 44]). More precisely, let us fix a scale parameter  $B > 1$ , and let  $b(u)$ ,  $u \in \mathbb{R}$ , be a positive kernel satisfying the following three assumptions:

1.  $b(\cdot)$  has compact support in  $[1/B, B]$ ;
2.  $b(\cdot)$  is infinitely differentiable in  $(0, \infty)$ ;
3. the following partition of unity property holds

$$\sum_{j=-\infty}^{\infty} b^2\left(\frac{u}{B^j}\right) = 1 , \text{ for all } u > 0 .$$

In Fig. (1) we show a visualization of  $b\left(\frac{\sqrt{e_{\ell, n}}}{B^j}\right)$  for different needlet frequency  $j$  values and  $e_{\ell, n} = n_{max} = 200$ .

Numerical recipes for the construction of window functions satisfying the three conditions above are now well-known to the literature; for instance, in [47] (see also [35]), the following procedure is introduced:

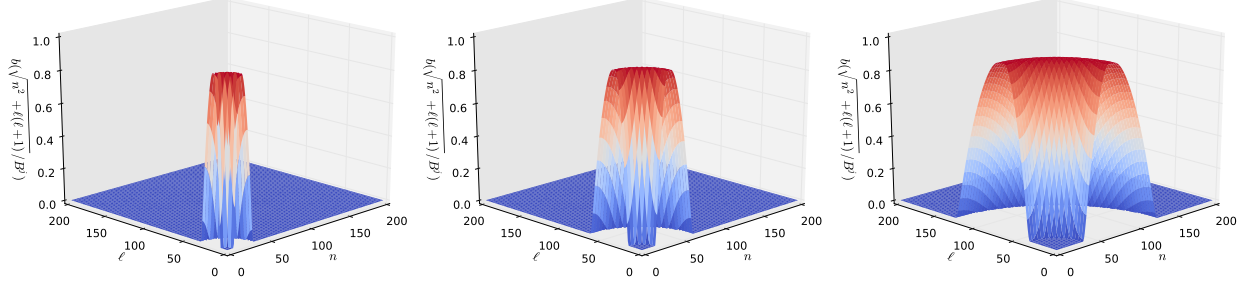


FIG. 1: 3D needlet window functions  $b\left(\frac{\sqrt{e_{\ell,n}}}{B^j}\right)$ :  $j = 4$  (left panel),  $j = 5$  (middle panel) and  $j = 6$  (right panel).

- STEP 1: Construct the  $C^\infty$ -function

$$\phi_1(t) = \begin{cases} \exp\left(-\frac{1}{1-t^2}\right) & t \in [-1, 1] \\ 0 & \text{otherwise} \end{cases},$$

compactly supported in  $[-1, 1]$ ;

- STEP 2: Implement the non-decreasing  $C^\infty$ -function

$$\phi_2(u) = \frac{\int_{-1}^u \phi_1(t) dt}{\int_{-1}^1 \phi_1(t) dt},$$

normalized in order to have  $\phi_2(-1) = 0$ ;  $\phi_2(1) = 1$ ;

- STEP 3: Construct the function

$$\phi_3(t) = \begin{cases} 1 & t \in [0, 1/B] \\ \phi_2\left(1 - \frac{2B}{B-1}\left(t - \frac{1}{B}\right)\right) & t \in (1/B, 1] \\ 0 & t \in (1, \infty) \end{cases};$$

- STEP 4: Define, for  $u \in \mathbb{R}$

$$b^2(u) = \phi_3\left(\frac{u}{B}\right) - \phi_3(u).$$

Now recall that  $e_{\ell,n} = n^2 + \ell(\ell + 1)$ , and let the symbol  $[\ell, n]_j$  denote the pairs of  $\ell$  and  $n$  such that  $e_{\ell,n}$  is bounded above and below respectively by  $B^{2(j+1)}$  and  $B^{2(j-1)}$ , i.e.

$$[\ell, n]_j = \left\{ l, n : B^{2(j-1)} \leq e_{\ell,n} \leq B^{2(j+1)} \right\}.$$

We have the following

**Definition 1** *The radial 3D-needlets basis is defined by*

$$\begin{aligned} \Phi_{j,q,k}(r, \vartheta, \varphi) &= \sqrt{\lambda_{j,q,k}} \sum_{[\ell,n]_j} \sum_{m=-\ell}^{\ell} b\left(\frac{\sqrt{e_{\ell,n}}}{B^j}\right) \\ &\quad \times \bar{u}_{\ell,m,n}(\xi_{j,q,k}) u_{\ell,m,n}(x), \end{aligned} \quad (\text{III.1})$$

where  $\lambda_{j,q,k}$  and  $\xi_{j,q,k}$  denote respectively the pixel volume and the pixel center.

Analogously to the related constructions on the sphere or on other manifolds, radial 3D-needlets can be viewed as the convolution of the projector operator

$$Z_{\ell n}(\xi_{j,q,k}, x) = \sum_m \bar{u}_{\ell,m,n}(x) u_{\ell,m,n}(\xi_{j,q,k})$$

with the window function  $b(\cdot)$ . The properties of this system are to some extent analogous to the related construction on the sphere, as illustrated below.

#### A. The tight frame property

Let us first recall the notion of tight frame, which is defined to be a countable set of functions  $\{e_i\}$  such that

$$\sum_i \beta_i^2(f) = \int_B f(x)^2 dx;$$

where the coefficients  $\beta_i(f)$  are defined by

$$\beta_i(f) = \int f(x) e_i(x) dx, \quad (\text{III.2})$$

so that the “energy” of the function  $f$  is fully conserved in the collection of  $\beta_i$ ’s; we refer for instance to [24, 43] and the references therein for more details and discussions. In words, a tight frame can be basically seen as a (possible redundant) basis; indeed we recall that tight frames enjoy the same reconstruction property as standard orthonormal systems, e.g.

$$f = \sum_i \beta_i(f) e_i,$$

the equality holding in the  $L^2$  sense.

It is a straightforward consequence of the previous construction that the set  $\{\Phi_{j,q,k}\}_{j,k,q}$  describes a tight frame over  $L^2(M, d\mu)$ , so that an exact reconstruction formula holds in this space; the details of the derivation of this result are collected in the Appendix. Indeed, let  $F \in L^2(M, d\mu)$ , i.e. the space of functions which have



finite norm  $\|\cdot\|_{L^2(M)}^2$ , where

$$\|F\|_{L^2(M,d\mu)}^2 := \int_0^{2\pi} \int_{S^2} F^2(r, \vartheta, \varphi) \sin \vartheta dr d\vartheta d\varphi . \quad (\text{III.3})$$

The 3D-needlet coefficients are defined as

$$\beta_{j,q,k} := \beta_{j,q,k}(F) = \int F \Phi_{j,q,k} d\mu,$$

or, more explicitly,

$$\begin{aligned} \beta_{j,q,k} &= \sqrt{\lambda_{j,q,k}} \sum_{[\ell,n]_j} \sum_{m=-\ell}^{\ell} b\left(\frac{\sqrt{e_{\ell,n}}}{B^j}\right) \\ &\times a_{\ell,m,n} u_{\ell,m,n}(\xi_{j,q,k}) , \end{aligned} \quad (\text{III.4})$$

where  $a_{\ell,m,n}$  is given by (II.7). The tight frame property then gives

$$\|F\|_{L^2(M,d\mu)}^2 = \sum_{j \geq 0} \sum_{q=1}^{Q_j} \sum_{k=1}^{K_j} |\beta_{j,q,k}|^2;$$

this property implies also the reconstruction formula

$$F(x) = \sum_{j \geq 0} \sum_{k=1}^{K_j} \sum_{q=1}^{Q_j} \beta_{j,q,k} \Phi_{j,q,k}(x) , \quad (\text{III.5})$$

see the Appendix for more discussion and some technical details.

There are some important statistical applications of the tight frame property. Firstly, the reconstruction property allows the implementation of denoising and image reconstruction techniques, for instance on the basis of the universally known thresholding paradigm (see for instance [4, 12, 26]); in view of the localization properties discussed in the following paragraph, such denoising techniques will enjoy statistical optimality properties, in the sense of minimizing the expected value of the reconstruction error, defined by

$$\mathbb{E} \left[ \left\| \widehat{F} - F \right\|_{L^2(M,d\mu)}^2 \right] = \mathbb{E} \left[ \int_M \left( \widehat{F}(x) - F(x) \right)^2 d\mu(x) \right]$$

Here  $\mathbb{E}[\cdot]$  denotes expected value and  $\widehat{F}$  the reconstructed function in the presence of additive noise with standard properties. It is important to stress that this reconstruction error is measured according to the norm introduced in (III.3), rather than the usual Euclidean measure in spherical coordinates, where integration is performed with respect to the factor  $r^2 \sin \vartheta dr d\vartheta d\varphi$ . In practical terms, this means that the observations at lower redshift are given a higher weight when performing image denoising; this appears a rather reasonable strategy, as most astrophysical catalogues are more complete and less noisy at lower redshift.

We also note that the tight frame property allows an estimator for the averaged power spectrum of random fields to be constructed by means of the squared needlet coefficients, along the same lines as for instance [3] in the spherical case. More details and further investigations on all these issues are left for future research.

## B. Localization Properties

It is immediately seen that the functions  $\{\Phi_{j,q,k}(\cdot)\}$  are compactly supported in the harmonic domain; indeed for any fixed  $j$ , as argued before we have that  $b(\cdot)$  is non-zero for  $u \in (B^{-1}, B)$ , and hence it follows that  $b\left(\frac{\sqrt{e_{\ell,n}}}{B^j}\right) \neq 0$  only for  $e_{\ell,n} \in [B^{2(j-1)}, B^{2(j+1)}]$ . For instance, for  $B = \sqrt{2}$  and  $j = 4$  we have  $8 \leq e_{\ell,n} \leq 32$ , allowing for the pairs

$$(\ell, n) = (1, 3), (1, 4), (1, 5), (2, 2), (2, 3), (2, 4), \dots, (5, 1) .$$

It is also easy to establish localization in the real domain by means of general results on localization of needlet-type constructions for smooth manifolds. In particular, it follows from Theorem 2.2 in [18], see also [42], that for all  $\tau \in \mathbb{N}$ , there exists constants  $c_\tau$  such that

$$|\Phi_{j,q,k}(x)| \leq \frac{c_\tau B^{\frac{3}{2}j}}{(1 + B^j d_M(x, \xi_{j,q,k}))^\tau} , \quad (\text{III.6})$$

uniformly over  $j, q, k$  and  $x$ . It is very important to notice that the distance at the denominator is provided by equation (II.3).

An important consequence of localization can be derived on the behaviour of the  $L^p$  norms for the functions  $\{\Phi_{j,q,k}(\cdot)\}$ . In particular, it can be proved by standard arguments (as for instance in [39]) that, for all  $1 \leq p < \infty$ ,

$$\|\Phi_{j,q,k}\|_{L^p(M,d\mu)}^p := \int_M |\Phi_{j,q,k}|^p(x) d\mu(x) \approx B^{\frac{3}{2}(p-2)j} , \quad (\text{III.7})$$

while

$$\|\Phi_{j,q,k}\|_{L^\infty(M,d\mu)} \approx B^{\frac{3}{2}j} .$$

The result is consistent with the general characterization for the  $L^p$ -norm of spherical needlets on  $S^d$ , which is well-known to be given by  $\|\psi_{j,k}\|_{L^p(S^d)}^p \approx B^{\frac{d}{2}(p-2)j}$ ; here of course  $d = 3$ . The proof is completely standard, and hence omitted; we only remark that this characterization of  $L^p$  properties plays a fundamental role when investigating the optimality of denoising and image reconstruction techniques based on wavelet thresholding, see again [4] for further references and discussion.

## IV. A COMPARISON WITH ALTERNATIVE CONSTRUCTIONS

The ingredients for the construction of localized tight frames on a compact manifold are now well-understood; one starts from a family of eigenfunctions and the associated projection kernel, then considers a window function to average these projectors over a bounded subset of frequencies, then proceeds to discretization by means of a suitable set of cubature points and weights, see for instance [17, 18, 38–41, 44]. The localization and tight

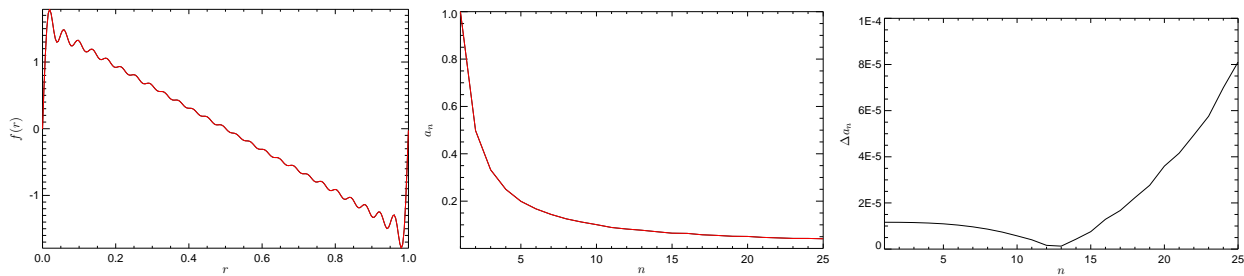


FIG. 2: Radial line synthesis and analysis: input (black curve) and reconstructed (red curve) function  $f(r)$  (left panel), original and reconstructed radial harmonic coefficient  $a_n$  (middle panel), difference between input and reconstructed  $a_n$  (right panel).

frame properties are then easy consequences of general results. A natural question then arises, e.g., what would be the alternative properties of a construction based on a different choice of eigenfunctions, corresponding for instance to the standard Laplacian in spherical coordinates (e.g., (II.2) rather than (II.1)). Indeed, a full system of eigenfunctions for the Laplacian in spherical coordinates is well-known to be given by

$$E_{\ell,m,k}(r,\omega) = \sqrt{\frac{2}{\pi}} \frac{J_{\ell+\frac{1}{2}}(kr)}{\sqrt{kr}} Y_{\ell,m}(\omega), \quad r \in [0, 1], \quad \omega \in S^2,$$

which can be discretized imposing the boundary conditions  $E_{\ell,m,k}(1,\omega) \equiv 0$ , yielding the family  $\{E_{\ell,m,k_{\ell_p}}(r,\omega)\}$ , for  $k_{\ell_p}$  the zeroes of the Bessel function  $J_{\ell+\frac{1}{2}}(\cdot)$  in the interval  $(0, 1)$ . Writing  $e(\ell, k_{\ell_p})$  for the corresponding set of eigenvalues, a needlet type construction would then lead to the following proposal:

$$\begin{aligned} \Psi_{j,q,k}(r,\omega) &= \sqrt{\lambda_{j,q,k}} \sum_{\ell,m} \sum_{k_{\ell_p}} b\left(\frac{\sqrt{e(\ell, k_{\ell_p})}}{B^j}\right) \\ &\times E_{\ell,m,k_{\ell_p}}(r,\omega) E_{\ell,m,k_{\ell_p}}(r_q, \omega_{j,k}), \end{aligned}$$

which is close to the starting point of the construction in [31], the main difference being that their weight function is actually a product of a radial and spherical part, and its argument is not immediately related to the eigenvalues of the summed eigenfunctions (see also [29] for 3D isotropic wavelets based on Bessel functions). It is then easy to show that  $\Psi_{j,q,k}(\cdot, \cdot)$  enjoys a related form of localization property, namely for all  $\tau \in \mathbb{N}$ , there exists constants  $c_\tau$  such that

$$|\Psi_{j,q,k}(x)| \leq \frac{c_\tau B^{\frac{3}{2}j}}{(1 + B^j d(x, \xi_{j,q,k}))^\tau}, \quad (\text{IV.1})$$

where  $x = (r, \omega)$ ,  $\xi_{j,q,k} = (r_q, \omega_{j,k})$  and  $d(\cdot, \cdot)$  denotes as before standard Euclidean distance. It is then important to stress the different merits of this construction, with respect to the one we focussed on earlier:

1) for the system  $\{\Psi_{j,q,k}\}$  distances are evaluated with a standard Euclidean metric, and the centre of the ball represents a mere choice of coordinates, e.g., the radial

part depends just on the choice of coordinated and does not necessarily correspond to a specific physical meaning

2) for the system  $\{\Phi_{j,q,k}\}$  distances are very much determined by the choice of the centre and the radial part does have a specific interpretation, e.g., the distance to the observer.

The rationale underlying 2) was already explained earlier in this paper; we envisage a situation where an observer located at the centre of a ball observes a surrounding Universe made up of concentric spheres having the same pixelizations. As a consequence "closer" spheres, e.g. those corresponding to smaller radii, are observed at the same angular resolution as more distant ones - in Euclidean coordinates, this obviously means that the sampling is finer. Our construction of radial needlets is simply reflecting this basic feature: as a consequence, for any given frequency needlets are more localized in proper distance for points located in spheres closer to the observer. This may appear quite rational, to the extent in which for these closer regions the signal-to-noise ratio is higher and hence the reconstruction may proceed to finer details than in the outer regions. The practical performance of these ideas is tested in the Section to follow.

## V. NUMERICAL EVIDENCE

In this Section we will describe the numerical implementation of the algorithm developed in this paper. As far as the spherical component is concerned, our code exploits the well-tested HEALpix pixelization code (cfr. [22]), while for the radial part we use an equidistant pixelization, which is extensively tested below. To investigate the numerical stability and precision properties of the construction we propose, we shall analyze an input band-limited function on the ball which we simulate using a radial and angular test power spectrum.

### A. Radial reconstruction

Given a function  $g \in L^2([0, 2\pi], dr)$ , we obtain its radial harmonic coefficients by decomposing it in terms of radial eigenfunctions, i.e. for  $n = 1, 2, \dots$

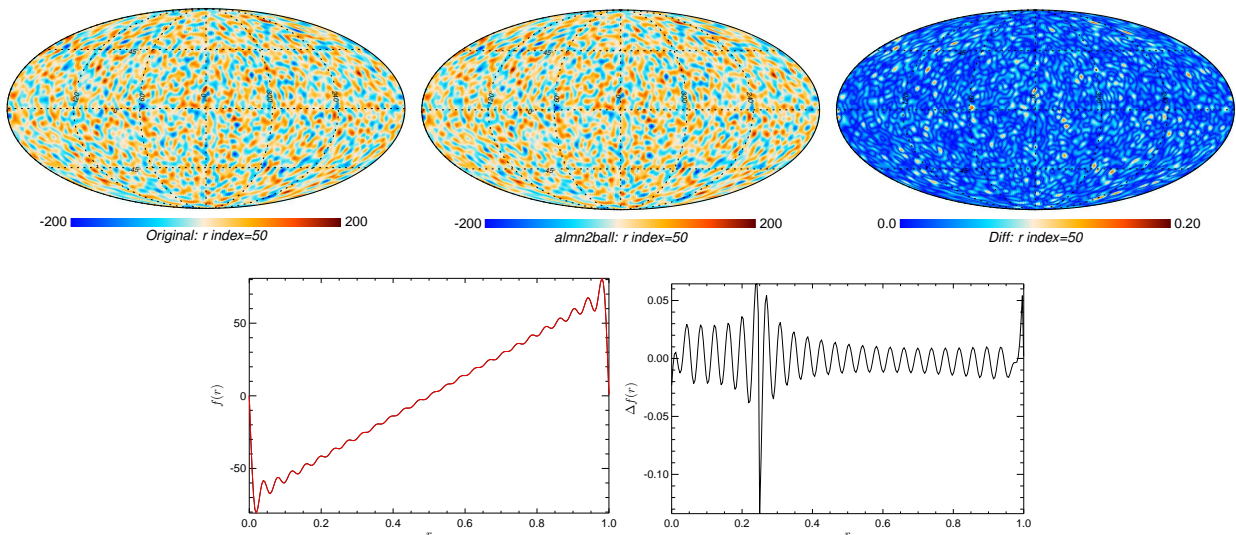


FIG. 3: Harmonic space synthesis and analysis: input function at the 51th shell (top left panel), reconstructed function at the 51th shell (top middle panel), difference between input and reconstructed functions at the 51th shell (top right panel), input and reconstructed radial function at the 201 HEALpix pixel (bottom left panel), and difference between input and reconstructed radial function at the 201 HEALpix pixel (bottom right panel).

$$a_n = \int_0^{2\pi} f(r) \frac{\exp(-inr)}{\sqrt{2\pi}} dr, \quad (\text{V.1})$$

The reconstruction of the input function can then be obtained via

$$f(r) = \sum_{n=0}^{\infty} a_n(f) \frac{\exp(inr)}{\sqrt{2\pi}}. \quad (\text{V.2})$$

By the standard Euler identity  $\exp(inr) = \cos nr + i \sin nr$ , the integral in (V.1) involves just sines and cosines function. The Filon-Simpson algorithm developed by [52] can solve such integral with arbitrary precision for an increasing radial grid.

To test our radial integration, we used as input the  $a_n$  coefficients shown in black curves in Fig. (2) and the reconstruction formula (V.2) to obtain  $f(r)$  which we evaluate at  $N_r = 256$  points. After performing the forward and backward transformation, the reconstructed  $g$  and  $a_n$  as well as their differences with respect to the input values are shown in red color curves in Fig. (2). The differences in the radial spectra are smaller than  $1e-4$  at all radial multipole values. This validates our radial analysis and synthesis routines.

## B. Discretization of functions on the unit ball

To describe the reconstruction of a band-limited function through the pixelization here introduced, we start from an angular power spectrum  $C_\ell$  which is derived from CAMB [32]  $\Lambda$ CDM 3D matter power spectrum at redshift

$z = 0.5$  and projected to 2D through Limber approximation; using Healpix, we then generated a set of random spherical harmonic coefficients from this power spectrum. We arbitrarily fixed the maximum angular multipole to  $\ell_{\max} = 65$ . For the radial component, we chose  $n_{\max} = 25$  and generated a set of Fourier coefficients  $a_n$  which are plotted in the middle box of Fig. (2). We then convolved the corresponding radial and spherical components to obtain the desired function on the 3D ball. Our test function  $f(r)$  is evaluated at  $N_r = 256$  radial points while the angular part is defined on HEALpix  $N_{\text{side}} = 64$  pixels.

Our numerical 3D grid has a total of  $N_r * 12 * N_{\text{side}}^2$  pixels. We stress again that our main interest here is to test the accuracy of the codes, so at this stage we are not concerned with the physical interest of the functions to be reconstructed; the analysis of more physically motivated models, such as for instance maps from  $N$ -body simulations will be reported in another paper.

In a similar spirit to the highly popular spherical algorithms proposed by [22], we have developed the ball equivalent of the HEALpix *alm2map* and *map2alm* codes, which are named *almn2ball* and *ball2almn*. These two routines, respectively, solve the analysis and synthesis equations of (II.7) and (II.6). Equivalently, we have *ball2beta* and *beta2ball* to solve equations (III.4) and (III.5), which are respectively performing needlet space analysis and synthesis. We have optimized these codes so that they are fast and run either in serial or parallel mode; we have fully exploited the rigorously tested and well known HEALpix routines, so that researchers familiar with HEALpix should find our code rather intuitive. The modularity of our code, moreover, means that



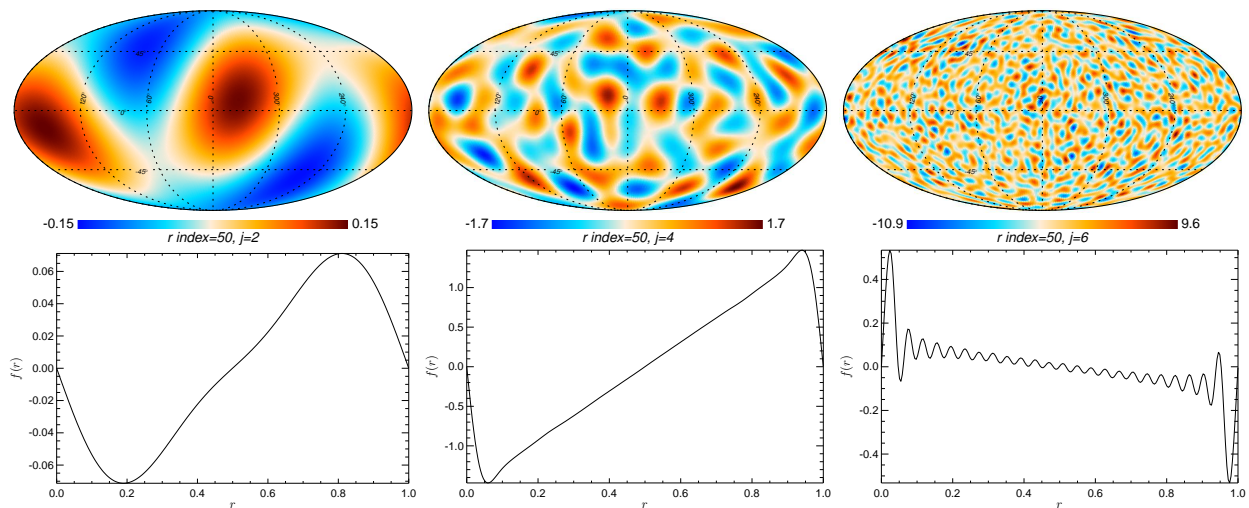


FIG. 4: 3D needlet component maps: the upper panel shows angular part of the corresponding needlet component map at the 51th shell while the lower panel is for the radial part at the 201 HEALpix pixel. The  $j^{\text{th}}$  component have a compact support of multipoles  $B^{j-1} < \sqrt{\ell(\ell+1) + n^2} < B^{j+1}$ .

adapting our routines to any other pixelization packages will be straightforward.

To test the accuracy of our code, both in harmonic and real space, in Fig. (3) we show the original and reconstructed function on the unit ball sliced at the 50th radial shell and the radial function at the 200th HEALpix pixel. It can be checked from the real-space difference plots in the same figure that the residuals are very small and comparable to HEALpix 's accuracy. The difference in harmonic space is such that both the radial and angular spectra are recovered with accuracy  $< 1e-4$  at all multipoles.

### C. Radial 3D needlet synthesis and analysis

Here we start from the  $a_{\ell,m,n}$  coefficients obtained from the previous section analysis and we compute the needlet coefficients  $\beta_{j,q,k}$  through our routine *almn2beta*, which implements (III.1). Optionally one can start directly from the discretization of the function on the ball and call *ball2beta* to get  $\beta_{j,q,k}$  directly. The needlet parameters we use in this analysis are  $j = 0, 1, \dots, N_j - 1$ ,  $q = 0, 1, \dots, Q_j$ ,  $n_k = 0, 1, \dots, K_j - 1$  where  $N_j = 7$ ,  $Q_j = N_r = 256$ , and  $K_j = 12 * 64^2$ . To reconstruct the function on the ball from the needlet coefficients we call *beta2ball*. The pixel by pixel and harmonic space accuracy of the function reconstructed from needlet coefficients are almost identical to that of the function reconstructed just from the  $a_{\ell,m,n}$  coefficients, thus providing some very reassuring evidence on the accuracy of the algorithm. As mentioned earlier, further evidence on simulations with more realistic experimental conditions is left to future research.

In Fig. (4), we show the needlet component maps. The  $j^{\text{th}}$  needlet component map have a compact support on

the range of combined radial and angular multipoles such that  $B^{j-1} < \sqrt{\ell(\ell+1) + n^2} < B^{j+1}$ .

### Appendix A: Some technical details

In this Appendix, we discuss the tight frame property which characterizes this construction. Indeed, let  $F \in L^2(M, d\mu)$ : the corresponding 3D-needlet coefficients are given by (III.4). For all  $1 \leq q \leq Q_j$ ,  $1 \leq k \leq K_j$ , we have

$$|\beta_{j,q,k}|^2 = \lambda_{j,q,k} \left| \sum_{[\ell,n]_j} \sum_{|m| \leq \ell} b \left( \frac{\sqrt{e_{\ell,n}}}{B^j} \right) a_{\ell,m,n} u_{\ell,m,n}(\xi_{j,q,k}) \right|^2.$$

From the spectral theorem (see for instance [10], cfr. also [44]) we have also, for  $F \in L^2(M, d\mu)$

$$\sum_{j \in \mathbb{Z}} \|b(B^{-j} \sqrt{\Delta_M}) F\|_{L^2(M, d\mu)}^2 = \|F\|_{L^2(M, d\mu)}^2,$$

where  $\|\cdot\|_{L^2(M)}$  denotes as usual the  $L^2$ -norm of the function which we recalled in (III.3). Let us introduce also the kernel

$$\mathcal{K}_j(x, x') := \sum_{[l,n]_j} \sum_{|m|=-l}^l b \left( \frac{\sqrt{e_{n,l}}}{B^j} \right) \bar{u}_{\ell,m,n}(x') u_{\ell,m,n}(x),$$

$x, x' \in M$ , from which we obtain the projections

$$\begin{aligned} F_j(x) &:= b(B^{-j} \sqrt{\Delta_M}) F = \langle \mathcal{K}_j(\cdot, x), F(\cdot) \rangle_{L^2(M, d\mu)} \\ &= \sum_{[\ell,n]_j} \sum_{|m|=-\ell}^{\ell} b \left( \frac{\sqrt{e_{\ell,n}}}{B^j} \right) a_{\ell,m,n} u_{\ell,m,n}(x). \end{aligned}$$

Next,

$$\begin{aligned} & \|F_j(x)\|_{L^2(M,d\mu)}^2 \\ &= \int_M \left| \sum_{[\ell,n]_j} \sum_{m=-\ell}^{\ell} b\left(\frac{\sqrt{e_{\ell,n}}}{B^j}\right) a_{\ell,m,n} u_{\ell,m,n}(x) \right|^2 d\mu(x). \end{aligned}$$

The integrand function clearly belongs to  $\Pi_{B^{2(j+1)}}$ , i.e. the space of functions which can be expressed as linear combinations of basis elements corresponding to eigenvalues smaller than  $B^{2(j+1)}$ . For these functions, an exact cubature formula holds, and we get

$$\|F_j(x)\|_{L^2(M,d\mu)}^2 = \sum_{q=1}^{Q_j} \sum_{k=1}^{K_j} \lambda_{j,q,k} |F_j(\xi_{j,q,k})|^2.$$

Therefore we have that

$$\begin{aligned} \|F\|_{L^2(M,d\mu)}^2 &= \sum_{j \geq 0} \|b(B^{-j} \sqrt{\Delta_M}) F\|_{L^2(M,d\mu)}^2 \\ &= \sum_{j \geq 0} \|F_j(x)\|_{L^2(M,d\mu)}^2 \\ &= \sum_{j \geq 0} \sum_{q=1}^{Q_j} \sum_{k=1}^{K_j} |\beta_{j,q,k}|^2, \end{aligned}$$

as claimed.

**Acknowledgement 1** *The authors thank R. Rosenfelder for sending us his Fortran 90 Filon-Simpson code.*

- 
- [1] **Aguilar, J. A., for the IceCube Collaboration (2013)**. Neutrino searches with the IceCube telescope. *Nucl. Phys. B Proc. Supp.* 237, pp. 250-252, [arXiv:1301.6504](#).
- [2] **ARGO-YBJ Collaboration (2013)**. TeV gamma-ray survey of the Northern sky using the ARGO-YBJ detector. *The Astrophysical Journal*, 779:27.
- [3] **Baldi, P., Kerkyacharian, G., Marinucci, D. and Picard, D. (2009)**. Asymptotics for Spherical Needlets. *Annals of Statistics*, Vol. 37, No. 3, pp. 1150-1171.
- [4] **Baldi, P., Kerkyacharian, G., Marinucci, D. and Picard, D. (2009)**. Adaptive density estimation for directional data using needlets. *Annals of Statistics*, Vol. 37, pp. 3362-3395.
- [5] **Bobin, J., Starck, J.-L., Sureau, J.-L., Basak S. (2012)**. Sparse component separation for accurate CMB map estimation. *Astronomy and Astrophysics*, 550, A73, [arXiv:1206.1773](#).
- [6] **Bobin, J., Sureau, F., Paykari P., Rassat, A., Basak, S., Starck, J. -L. (2013)**. WMAP 9-year CMB estimation using sparsity. *Astronomy and Astrophysics*, 553, L4, pp 10, [arXiv:1303.4881](#).
- [7] **Casaponsa, B., Barreiro, R. B., Curto A., Martínez-González, E., Vielva P. (2011)**. Wilkinson Microwave Anisotropy Probe 7-yr constraints on fNL with a fast wavelet estimator. *Mon.Not.Roy.Astron.Soc.*, 411 2019C.
- [8] **Cruz, M., Martinez-Gonzalez, E., Vielva, P., Cayon L. (2005)**. Detection of a non-Gaussian Spot in WMAP. *Mon.Not.Roy.Astron.Soc.* 356:29-4.
- [9] **Das S. et al. (2011)**. Detection of the Power Spectrum of Cosmic Microwave Background Lensing by the Atacama Cosmology Telescope. *Physical Review Lett.* 107, 021301.
- [10] **Davies, E. B., (1996)**. *Spectral Theory and Differential Operators*. Cambridge University Press.
- [11] **Delabrouille, J., Cardoso, J.-F., Le Jeune, M., Betoule, M., Faÿ, G., Guilloux, F. (2009)**. A full sky, low foreground, high resolution CMB map from WMAP. *Astronomics and Astrophysics*, Vol. 493, Issue 3, pp. 835-857.
- [12] **Donoho, D., Johnstone, I., Kerkyacharian, G., Picard, D. (1996)** Density estimation by wavelet thresholding, *Annals of Statistics*, Vol. 24, pp. 508-539.
- [13] **Donzelli, S., Hansen, F. K., Liguori, M., Marinucci, D. and Matarrese, S. (2012)** On the linear term correction for needlets/wavelets non-Gaussianity estimators, *Astrophysical Journal* 755, no. 19, [arXiv:1202.1478](#).
- [14] **Faÿ, G., Delabrouille J., Kerkyacharian, G., Picard, (2013)**, Testing the isotropy of high energy cosmic rays using spherical needlets. *Annals of Applied Statistics*, Vol. 7, No. 2, pp. 1040-1073
- [15] **Fengler, M., Michel, D., Michel, V. (2006)**. Harmonic spline-wavelet on 3 dimensional ball and their applications to the reconstruction of the earth's density distribution from gravitational data at arbitrarily shaped satellite orbits. *ZAMM - Journal of Applied Mathematics and Mechanics/Zeitschrift fr Angewandte Mathematik und Mechanik*, Vol. 86, n. 11, pp. 856-973.
- [16] **Fermi-LAT collaboration, Fermi-GBM collaboration(2013)**. Fermi-LAT Observations of the Gamma-ray Burst GRB 130427A. *Science* 3, Vol. 343 no. 6166 pp. 42-47, [arXiv:1311.5623](#).
- [17] **Geller, D. and Mayeli, A. (2009)**, Continuous Wavelets on Manifolds, *Math. Z.*, Vol. 262, pp. 895-927, [arXiv: math/0602201](#)
- [18] **Geller, D. and Mayeli, A. (2009)** Nearly Tight Frames and Space-Frequency Analysis on Compact Manifolds, *Math. Z.*, Vol, 263 (2009), pp. 235-264, [arXiv: 0706.3642](#)
- [19] **Geller, D. and Marinucci, D. (2010)** Spin wavelets on the sphere *J. Fourier Anal. Appl.*, Vol, 6 (2009), pp. 840-884, [arXiv: 0811.2935](#)
- [20] **Geller, D. and Hansen, F. K. and Marinucci, D. and Kerkyacharian, G. and Picard, D. (2008)** Spin needlets for cosmic microwave background polarization data analysis *Phys. Rev. D* Vol, 78 (2008), pp. 123533, [arXiv: 0811.2881](#)
- [21] **Giuliani A. et al. (2010)**. AGILE detection of GeV gamma-ray emission from the SNR W28. *Astronomy and Astrophysics*, 516, L11.
- [22] **Gorski, K. M. , Hivon, E., Banday, A. J., Wandelt, B. D., Hansen F. K., Reinecke, M., Bartelman M. (2005)**. HEALPix – a Framework for High Resolution Discretization, and Fast Analysis of Data Dis-

- tributed on the Sphere. *The Astrophysics Journal*, 622, pp. 759-771.
- [23] **Hanson D. et al. (SPTpol Collaboration) (2013)**. Detection of B-Mode Polarization in the Cosmic Microwave Background with Data from the South Pole Telescope. *Phys. Rev. Lett.* 111, 141301.
- [24] **Hernandez E., Weiss, G. (1996)**. *A first course on wavelets*. CRC press, USA.
- [25] **Iuppa R., Di Sciacio, G., Hansen, F.K., Marinucci, D., Santonico, R. (2011)**. A needlet-based approach to the shower-mode data analysis in the ARGOS-YSB experiment. *Nuclear Instruments and Methods in Physics Research Section A Accelerators Spectrometers Detectors and Associated Equipment 01/2011*; 692:170-173.
- [26] **Hardle, W., Kerkycharian, G. Picard, D., Tsybakov, A. (1997)** *Wavelets, Approximations and statistical application*. Springer, Berlin
- [27] **Khalid, Z., Kennedy, R. A., McEwen, J. D. (2014)**. Slepian Spatial-Spectral Concentration on the Ball. Preprint [arXiv:1403.5553](https://arxiv.org/abs/1403.5553).
- [28] **Lan, X., Marinucci, D. (2008)**. The Needlets Bispectrum. *Electronic Journal of Statistics*, 2, 332-367.
- [29] **Lanusse, F., Rassat, A., Starck, J.L. (2012)**. Spherical 3D Isotropic Wavelets. *Astronomy and Astrophysics*, 540, A9.
- [30] **Laureijs, R., Duvet, L., Escudero Sanz, I., Gondoin, P., Lumb, D. H., Oosterbroek T.; Saavedra Criado G. (2010)**. The Euclid Mission. *SPIE Proceedings Vol. 7731*.
- [31] **Leistedt, B., McEwen, J. D. (2012)**. Exact Wavelets on the Ball. *IEEE Transactions on Signal Processing*, Vol. 60, no. 12.
- [32] **Lewis, A., Challinor, A., Lasenby, A. (2000)**. Efficient computation of CMB anisotropies in closed FRW models. *Astrophysical Journal* 538, pp. 473-476-.
- [33] **McEwen, J. D., Vielva, P., Wiaux, Y., Barreiro, R. B., Cayón, I., Hobson, M. P., Lasenby, A. N., Martínez-González, E. and Sanz, J. L. (2007)** Cosmological Applications of a Wavelet Analysis on the Sphere. *J. Fourier Anal. Appl. Vol. 13, no. 4, pp. 495-510*.
- [34] **Marinucci, D., Pietrobon, D., Balbi, A., Baldi, P., Cabella, P., Kerkycharian, G., Natoli, P., Picard, D., Vittorio N. (2008)**. Spherical Needlets for CMB Data Analysis. *Monthly Notices of the Royal Astronomical Society*, Vol. 383, Is. 2, pp. 539-545.
- [35] **Marinucci, D. and Peccati, G.(2011)**. *Random Fields on the Sphere. Representation, Limit Theorem and Cosmological Applications*. Cambridge Univ. Pr.
- [36] **Michel V. (2005)**. Wavelets on the 3 dimensional ball. *PAMM*, Vol. 5, no. 1, pp. 775-776.
- [37] **Modest Z., Räth, C., Banday, A. J., Rossmanith, G., Sütterlin, R., Basak, S., Delabrouille, J., Górski, K. M., Morfill G. E. (2012)**. Scale dependent non-Gaussianities in the CMB data identified with Minkowski Functionals and Scaling Indices. *Mon.Not.Roy.Astron.Soc.*, 09, 428(1).
- [38] **Narcowich, F.J., Petrushev, P. and Ward, J.D. (2006a)** Localized Tight Frames on Spheres, *SIAM Journal of Mathematical Analysis* Vol. 38, pp. 574-594.
- [39] **Narcowich, F.J., Petrushev, P. and Ward, J.D. (2006b)** Decomposition of Besov and Triebel-Lizorkin Spaces on the Sphere, *Journal of Functional Analysis*, Vol. 238, 2, 530-564.
- [40] **Pesenson, I. Z. (2000)**. A sampling theorem on homogeneous manifolds. *Trans. Amer. Math. Soc.* 352 (2000), no. 9, pp. 4257-4269.
- [41] **Pesenson, I. Z. (2004)**. Poincare-type inequalities and reconstruction of Paley Wiener functions on manifolds. *J. of Geometric Analysis*, (4), 1, pp. 101-121.
- [42] **Pesenson, I. Z., Geller, D. (2013)**. Cubature formulas and discrete fourier transform on compact manifolds. *Dev. Math.*, 28, 431-453.
- [43] **Pesenson, I. Z. (2014)**. Splines and Wavelets on Geophysically Relevant Manifolds. *Handbook of Geomatics, Springer*
- [44] **Pesenson, I. Z. (2014)**.  $\varphi$ -transform on domains. *arxiv:1208.5165*.
- [45] **Petrushev, P., Xu, Y. (2006)**. Localized Polynomial Frames on the Ball, *Constr. Approx.* 27 (2008), 121-148.
- [46] **Pierre Auger Collaboration (2013)**. Bounds on the density of sources of ultra-high energy cosmic rays from the Pierre Auger Observatory. *JCAP*, 1305, 009.
- [47] **Pietrobon, D., Balbi, A., Marinucci, D. (2006)**. Integrated Sachs-Wolfe effect from the cross correlation of WMAP3 year and the NRAO VLA sky survey data: New results and constraints on dark energy. *Phys. Rev. D* 74, 043524.
- [48] **Pietrobon, D., Amblard, A., Balbi, A., Cabella, P., Cooray, A., Marinucci, D. (2008)**. Needlet Detection of Features in WMAP CMB Sky and the Impact on Anisotropies and Hemispherical Asymmetries, *Physical Review D*, D78 103504, *arXiv: 0809.0010*.
- [49] **Planck Collaboration (2013)**. Planck 2013 results. XXIII. Isotropy and statistics of the CMB. *Accepted for publication in A&A*.
- [50] **Regan, D., Mukherjee, P., Seery D. (2013)**. General CMB bispectrum analysis using wavelets and separable modes. *Phys. Rev. D* 88, 043512.
- [51] **Remazeilles, M., Delabrouille, J., Cardoso J.-F. (2011)**. Foreground component separation with generalised ILC. *Mon.Not.Roy.Astron.Soc.*, 418(1), pp. 467-476.
- [52] **Rosenfolder, R. (2006)**. On the Numerical Evaluation of a Class of Oscillatory Integrals in Worldline Variational Calculations. *ArXiv:hep-ph/0603161*
- [53] **Rudjord, O., Hansen, F.K., Lan, X., Liguori, M. Marinucci, D., Matarrese, S. (2009)**. An Estimate of the Primordial Non-Gaussianity Parameter  $f_{NL}$  Using the Needlet Bispectrum from WMAP, *Astrophysical Journal*, Volume 701, Issue 1, pp. 369-376, *arXiv:0901.3154*.
- [54] **Scodeller, S. Hansen, F.K., Marinucci, D. (2012)**. Detection of new point sources in WMAP 7 year data using internal templates and needlets. *ApJ*, 753, 27.
- [55] **Schmitt, J., Starck, J.L., Casandjian, J.M., Fadili, J., Grenier, I. (2012)**. Multichannel Poisson Denoising and Deconvolution on the Sphere : Application to the Fermi Gamma Ray Space Telescope. *Astronomy and Astrophysics*, 546, id.A114, pp10.
- [56] **Springel V. et al. (2005)**. Simulating the joint evolution of quasars, galaxies and their large-scale distribution. *Nature* 435:629-636.
- [57] **Starck, J.-L., Moudden, Y., Abrial P., Nguyen, M. (2006)**. Wavelets, Ridgelets and Curvelets on the Sphere, *Astronomy and Astrophysics*, 446, 1191-1204.
- [58] **Starck, J.-L., Moudden, Y., Bobin, J. (2009)**. Po-

- larized Wavelets and Curvelets on the Sphere. *Astronomy and Astrophysics*, 497, pp 931–943.
- [59] **Starck, J.-L., Murtagh, F. and Fadili, J. (2010)**. *Sparse Image and Signal Processing: Wavelets, Curvelets, Morphological Diversity*, Cambridge University Press.
- [60] **P. Vielva, J.L. Sanz (2010)**. Constraints on  $f_{NL}$  and  $g_{NL}$  from the analysis of the N-pdf of the CMB large scale anisotropies. *Mon.Not.Roy.Astron.Soc.*, 404(2), pp. 895-907.